Electronic Supplementary Information

Tuning the Reactivity of Mononuclear Nonheme Manganese(IV)-Oxo Complexes by Triflic Acid

Junying Chen,[a] Heejung Yoon,[b] Yong-Min Lee,[a] Mi Sook Seo,[a] Ritimukta Sarangi,[c] Shunichi Fukuzumi*[a,b] and Wonwoo Nam*[a]

[a]*Department of Chemistry and Nano Science and Centre for Biomimetic Systems, Ewha Womans University, Seoul 120-750, Korea*

[b]*Department of Material and Life Science, Graduate School of Engineering, ALCA, Japan Science and Technology Agency (JST), Osaka University, Suita, Osaka 565-0871, Japan*

[c]*Stanford Synchrotron Radiation Lightsource, SLAC National Accelerator Laboratory, Menlo Park, California 94025, United States*

*To whom correspondence should be addressed.

E-mail: wwnam@ewha.ac.kr, fukuzumi@chem.eng.osaka-u.ac.jp

Electronic Supplementary Information S1

Experimental section

Materials. Commercially available chemicals were used without further purification unless otherwise indicated. Solvents were dried according to published procedures and distilled under Ar prior to use.[S1] Trifluoromethanesulphonic acid (HOTf, OTf = $CF_3SO_3^-$) was purchased from Aldrich and used as received. $H_2^{18}O$ (95% ^{18}O-enriched) was purchased from ICON Services Inc. (Summit, NJ, USA). Iodosylbenzene (PhIO), N4Py and Bn-TPEN ligands, and $Mn^{II}(OTf)_2 \cdot 2CH_3CN$ were prepared by literature methods.[S2-S5] $[(L)Mn^{II}(CF_3SO_3)]^+$ and $[(L)Mn^{IV}(O)]^{2+}$ were prepared by literature methods.[S6-S8] One-electron reductants, such as $[Fe^{II}(Me_2\text{-}bpy)_3]^{2+}$, $[Fe^{II}(phen)_3]^{2+}$, $[Fe^{II}(bpy)_3]^{2+}$, $[Ru^{II}(Me_2\text{-}bpy)_3]^{2+}$, $[Ru^{II}(bpy)_3]^{2+}$, $[Ru^{II}(5\text{-}Cl\text{-}phen)_3]^{2+}$, $[Ru^{II}(5\text{-}Br\text{-}bpy)_3]^{2+}$ and $[Ru^{II}(5\text{-}NO_2\text{-}phen)_3]^{2+}$, were synthesized according to literature methods.[S9]

Instrumentation. UV-vis spectra were recorded on a Hewlett Packard 8453 diode array spectrophotometer equipped with a UNISOKU Scientific Instruments Cryostat USP-203A for low-temperature experiments or on a Hi-Tech Scientific (U.K.) SF-61 DX2 cryogenic stopped-flow spectrophotometer equipped with a Xe arc lamp and a KinetaScan diode array rapid scanning unit. The cold-spray ionization time-of-flight mass (CSI-TOF MS) spectral data were collected on a JMS-T100CS (JEOL) mass spectrometer equipped with the CSI source. Typical measurement conditions are as follows: needle voltage: 2.2 kV, orifice 1 current: 50-500 nA, orifice 1 voltage: 0 to 20 V, ring lens voltage: 10 V, ion source temperature: 5°C, spray temperature: –40 °C. X-band EPR spectra were recorded at 5 K using X-band Bruker EMX-plus spectrometer equipped with a dual mode cavity (ER 4116DM). Low temperature was achieved and controlled with an Oxford Instruments ESR900 liquid He quartz cryostat with an Oxford Instruments ITC503 temperature and gas flow controller. The experimental parameters for EPR measurement were as follows: Microwave frequency = 9.646 GHz, microwave power = 1.0 mW, modulation amplitude = 10 G, gain = 1×10^3, modulation frequency = 100 kHz, time constant = 40.96 ms, and conversion time = 81.00 ms. ^1H

NMR spectra were measured with a Bruker model digital AVANCE III 400 FT-NMR spectrometer.

EXAFS measurements. The Mn K-edge X-ray absorption spectra of **3**, $[(N4Py)Mn^{IV}(O)]^{2+}$−(HOTf)$_2$, were measured at the Stanford Synchrotron Radiation Lightsource (SSRL) on the unfocussed 20-pole 2 T wiggler side-station beam line 7-3 under standard ring conditions of 3 GeV and ~500 mA. A Si(220) double crystal monochromator was used for energy selection. A Rh-coated harmonic rejection mirror was used on beam line 7-3 to reject components of higher harmonics. The monochromator was further detuned by 70% to eliminate higher harmonic and to reduce beam damage on samples. The solution samples for $[(N4Py)Mn^{IV}(O)]^{2+}$−(HOTf)$_2$ (~120 μL) were transferred into 2 mm delrin XAS cells with 70 m Kapton tape windows under synthesis conditions and were immediately frozen after preparation and stored under liquid N$_2$. During data collection, samples were maintained at a constant temperature of ~10 – 15 K using an Oxford Instruments CF 1208 liquid helium cryostat. Data were measured to $k = 12$ Å^{-1} (fluorescence mode) using a Canberra Ge 30-element array detector. Internal energy calibration was accomplished by simultaneous measurement of the absorption of a Mn-foil placed between two ionization chambers situated after the sample. The first inflection point of the foil spectrum was fixed at 6539.0 eV. Data presented here are 32-scan average spectra for $[Mn^{IV}(O)]^{2+}$−(HOTf)$_2$. Data were processed by fitting a second-order polynomial to the pre-edge region and subtracting this from the entire spectrum as background. A four-region spline of orders 2, 3, 3 and 3 was used to model the smoothly decaying post-edge region. The data were normalized by subtracting the cubic spline and assigning the edge jump to 1.0 at 6555 eV using the Pyspline[S10] program. Data were then renormalized in Kaleidagraph for comparison and quantitation purposes. Theoretical EXAFS signals $\chi(k)$ were calculated by using FEFF[S11-13] (macintosh version). Starting structural models for $Mn^{IV}(O)$−(HOTf)$_2$ was generated by modifying the crystal structure[6] of $[Mn^{II}(N4Py)(CF_3SO_3)]^+$ in Avogadro.[S14] The input structure

was improved based on preliminary EXAFS fit parameters to generate more accurate theoretical EXAFS signals. Data fitting was performed in EXAFSPAK.[S15] The structural parameters varied during the fitting process were the bond distance (R) and the bond variance σ^2, which is related to the Debye-Waller factor resulting from thermal motion, and static disorder of the absorbing and scattering atoms. The non-structural parameter E_0 (the energy at which $k = 0$) was also allowed to vary but was restricted to a common value for every component in a given fit. Coordination numbers were systematically varied in the course of the fit but were fixed within a given fit.

EXAFS data analysis. The k^3 weighted Mn K-edge EXAFS data for **3**, along with their non-phase shift corrected Fourier transforms (FT) ($k = 1 - 12$ Å^{-1}), are shown in Figure 3. The EXAFS data for $[(N4Py)Mn^{IV}(O)]^{2+}$ (**1**) have been previously reported,[S6] but were re-measured under the same experimental conditions for direct comparison to proton bound $Mn^{IV}(O)$ complex. FEFF fits to the EXAFS data (Table S1 in SI) were performed to quantitatively understand the differences visually observed in the FT data. It is consistent with a distorted six-coordinate first shell with one short Mn−O (1.74 Å) which is longer than the 1.67 Å observed in $[(N4Py)Mn^{IV}(O)]^{2+}$ (**1**).

Kinetic measurements. Kinetic measurements were performed on a UNISOKU RSP-601 stopped-flow spectrometer equipped with a MOS-type highly sensitive photodiode array or a Hewlett Packard 8453 photodiode-array spectrophotometer at 298 K. Rates of electron transfer from one-electron donors to $[(N4Py)Mn^{IV}(O)]^{2+}−(HOTf)_2$ (**3**) and oxidation of *para*-X-thioanisoles (X = Me, H, F and Br) by **3** were monitored by the formation of absorption bands due to the one-electron oxidized species and the decay of absorption band due to **3**. Most kinetic measurements were carried out under pseudo-first-order conditions, where concentrations of substrates were maintained to be more than 10-folds excess of that of **3**. Because electron transfer from Ru(Me$_2$-bpy)$_3$]$^{2+}$ to **3** was too fast to follow even with stopped-flow equipment under pseudo-first-order conditions, the second-order rate constant was determined under second-order conditions, where the concentrations of

$[Ru^{II}(Me_2\text{-}bpy)_3]^{2+}$ and **3** were maintained as the same (1.0×10^{-4} M).

Redox titrations. Electron transfer from $[Ru^{II}(5\text{-}NO_2\text{-}phen)_3]^{2+}$ to $[(L)Mn^{IV}(O)]^{2+}-(HOTf)_2$ (5×10^{-4} M) was examined from the spectral change in various concentrations of $[Ru^{II}(5\text{-}NO_2\text{-}phen)_3]^{2+}$ (1×10^{-4} M $- 1 \times 10^{-3}$ M) at 273 K using a Hewlett Packard 8453 photodiode-array spectrometer. Typically, a deaerated CH_3CN solution of $[Ru^{II}(5\text{-}NO_2\text{-}phen)_3]^{2+}$ (1×10^{-4} M $- 1 \times 10^{-3}$ M) was added to a solution of **3** (5×10^{-4} M) in $CF_3CH_2OH\text{-}CH_3CN$ (*v/v* = 1:1). The concentration of $[Ru^{III}(5\text{-}NO_2\text{-}phen)_3]^{3+}$ was determined from the absorption band at λ_{max} = 650 nm due to $[Ru^{III}(5\text{-}NO_2\text{-}phen)_3]^{3+}$ ($\varepsilon = 1.3 \times 10^3$ M^{-1} cm^{-1}) and the ε value of $[Ru^{III}(5\text{-}NO_2\text{-}phen)_3]^{3+}$ was determined by the electron-transfer oxidation of $[Ru^{II}(5\text{-}NO_2\text{-}phen)_3]^{2+}$ with cerium (IV) ammonium nitrate (3 equiv) in the presence of HOTf (30 mM) in $CF_3CH_2OH\text{-}CH_3CN$ (*v/v* = 1:1) at 273 K.

Product analysis. Products formed in the oxidation of thioanisole by **3** were analyzed by HPLC. Quantitative analysis was performed by comparing the HPLC peak integration of products with its authentic sample. Methyl phenyl sulfoxide was produced as a sole product with 91(4)% yield (based on the concentration of catalyst). In the oxidation of 1,4-cyclohexadiene by **3**, GC and GC-MS were used to analyze products. Benzene was obtained as the sole product with the yield of 48(4)%, as observed in the oxidation of CHD by other metal-oxo complexes including $[(N4Py)Mn^{IV}(O)]^{2+}$, and $[(N4Py)Mn^{IV}(O)]^{2+}-(Sc^{3+})_2$.[S6]

References

S1. W. L. F. Armarego and C. L. L. Chai, *Purification of Laboratory Chemicals*, 6th ed.; Pergamon Press: Oxford, 2009.

S2. J. Kaizer, E. J. Klinker, N. Y. Oh, J.-U. Rohde, W. J. Song, A. Stubna, J. Kim, E. Münck, W. Nam and L. Que, Jr, *J. Am. Chem. Soc.*, 2004, **126**, 472.

S3. H. Saltzman and J. G. Sharefkin, Eds.; *Organic Syntheses*; Wiley: New York, 1973, Vol. V, p 658.

S4.   N. E. Dixon, G. A. Lawrance, P. A. Lay, A. M. Sargeson and H. Taube, *Inorg. Synth*., 1990, **28**, 70.

S5.   (a) M. Lubben, A. Meetsma, E. C. Wilkinson, B. Feringa and L. Que, Jr, *Angew. Chem., Int. Ed.,* 1995, **34**, 1512; (b) L. Duelund, R. Hazell, C. J. McKenzie, L. P. Nielsen and H. Toftlund, *J. Chem. Soc., Dalton Trans.,* 2001, 152; (c) S. Groni, P. Dorlet, G. Blain, S. Bourcier, R. Guillot and E. Anxolabéhère-Mallart, *Inorg. Chem.,* 2008, **47**, 3166.

S6.   J. Chen, Y.-M. Lee, K. M. Davis, X. Wu, M. S. Seo, K.-B. Cho, H. Yoon, Y. J. Park, S. Fukuzumi, Y. N. Pushkar and W. Nam, *J. Am. Chem. Soc.,* 2013, **135**, 6388.

S7.   H. Yoon, Y.-M. Lee, X. Wu, K.-B. Cho, R. Sarangi, W. Nam and S. Fukuzumi, *J. Am. Chem. Soc.,* 2013, **135**, 9186.

S8.   (a) X. Wu, M. S. Seo, K. M. Davis, Y.-M. Lee, J. Chen, K.-B. Cho, Y. N. Pushkar and W. Nam, *J. Am. Chem. Soc.,* 2011, **133**, 20088; (b) H. Yoon, Y. Morimoto, Y.-M. Lee, W. Nam and S. Fukuzumi, *Chem. Commun.,* 2012, **48**, 11187.

S9.   (a) O. Fussa-Rydel, H.-T. Zhang, J. T. Hupp and C. R. Leidner, *Inorg. Chem.,* 1989, **28**, 1533; (b) S. Fukuzumi, I. Nakanishi, K. Tanaka, T. Suenobu, A.Tabard, R. Guilard, E. Van Caemelbecke and K. M. Kadish, *J. Am. Chem. Soc.,* 1999, **121**, 785; (c) C-T. Lin, W. Bottcher, M. Chou, C. Creutz and N. Sutin, *J. Am. Chem. Soc.,* 1976, **98**, 6536.

S10. A. Tenderholt, B. Hedman and K. O. Hodgson, *PySpline: A Modern, Cross-Platform Program for the Processing of Raw Averaged XAS Edge and EXAFS Data; X-ray Absorption Fine Structure - XAFS13*, 2007, **882**, 105.

S11. S. I. Zabinsky, J. J. Rehr, A. Ankudinov, R. C. Albers and M. J. Eller, *Phys. Rev. B: Condens. Matter,* 1995, **52**, 2995.

S12. J. Mustre de Leon, J. J. Rehr, S. I. Zabinsky and R. C. Albers, *Phys. Rev. B: Condens. Matter,* 1991, **44**, 4146.

S13. J. J. Rehr, J. Mustre de Leon, S. I. Zabinsky and R. C. Albers, *J. Am. Chem. Soc.,* 1991, **113**, 5135.

S14. *Avogadro: an open-source molecular builder and visualization tool.* Version 1.1.0. http://avogadro.openmolecules.net/.

S15. G. N. George, *EXAFSPAK and EDG-FIT*, Stanford Synchrotron Radiation Laboratory, Stanford Linear Accelerator Center, Stanford, CA, 2000.

Table S1 EXAFS least squares fitting results for **3**

complex	coordination/path	R(Å)^a	σ^2(Å^2)^b	E_0 (eV)	F^c
	1 Mn-O	1.74	331		
	5 Mn-N	2.00	747		
	6 Mn-C	2.96	1326		
3	8 Mn-C-N	3.16	264	-3.53	0.26
	8 Mn-C-N	3.33	/264^d		
	8 Mn-C	4.25	914		
	6 Mn-C-N	4.71	233		

^{a}The estimated standard deviations for the distances are in the order of ± 0.02 Å. ^{b}The σ^2 values are multiplied by 10^5. ^{c}Error is given by $\Sigma[(\chi_{obsd} - \chi_{calcd})^2 k^6]/\Sigma[(\chi_{obsd})^2 k^6]$. $^{d/}$ indicates the σ^2 value for the path is linked to the preceding path. The S_0^2 factor was set at 0.95.

Table S2 Mn-O and Mn-N distances (Å) determined by EXAFS measurements

coordination/path	1	$(N4Py)Mn^{IV}(O)-(Sc^{3+})_2$	3
Mn-O	1.70^a $(1.67)^{b,c}$	1.74^a $(1.74)^{a,b}$	1.74
Mn-N$_{avg}$^{d}	2.00^a $(2.01)^{b,c}$	2.00^a $(2.01)^{a,b}$	2.00

[a]Taken from ref. 23 in Text. [b]The values in parenthesis were determined by DFT calculation. [c]Taken from reference, K.-B. Cho, S. Shaik and W. Nam, *J. Phys. Chem. Lett.*, 2012, **3**, 2851. [d]Average value of Mn-N distances.

Table S3 One-electron reduction potentials (E_{red}) of **3** (0.50 mM) in the presence of various concentrations of HOTf in CF_3CH_2OH-CH_3CN (v/v = 1:1) at 273 K

[HOTf], mM	E_{red} $vs.$ SCE, V
10	1.50
20	1.61
30	1.65
50	1.65
80	1.65
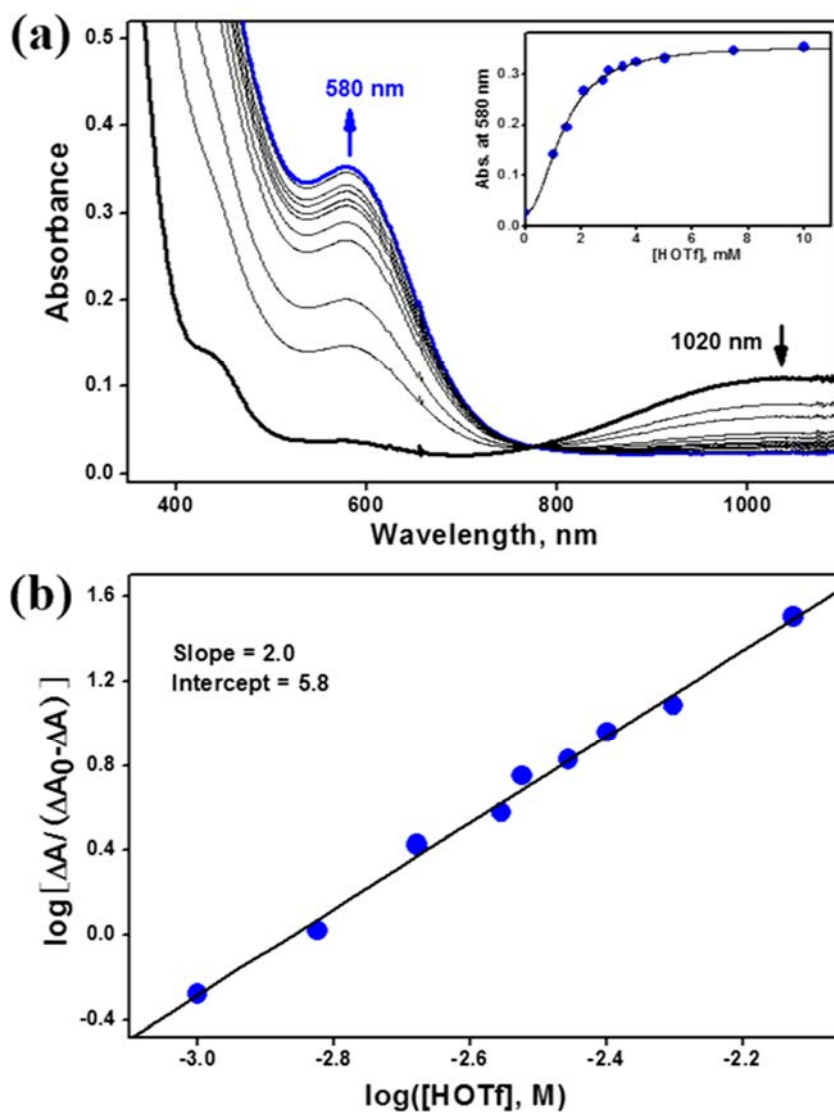
Fig. S1 (a) UV-vis spectral changes observed in the titration of **2** (black bold line) with H$^+$ upon addition of HOTf (0 – 10 mM) into the solution of **2** (0.50 mM) in CF$_3$CH$_2$OH-CH$_3$CN (*v/v* = 1:1) at 273 K. Inset shows the spectral titration monitored at 580 nm (blue circles) due to the formation of **4**. (b) Plot of log(ΔA/(ΔA$_0$ − ΔA)) against log[HOTf] in the spectral titration of **2** with HOTf. ΔA and ΔA$_0$ are the absorption change and final absorption change due to binding of n molecules of HOTf to **2** (see eqn (1) and (2) in Text).

Electronic Supplementary Information S10
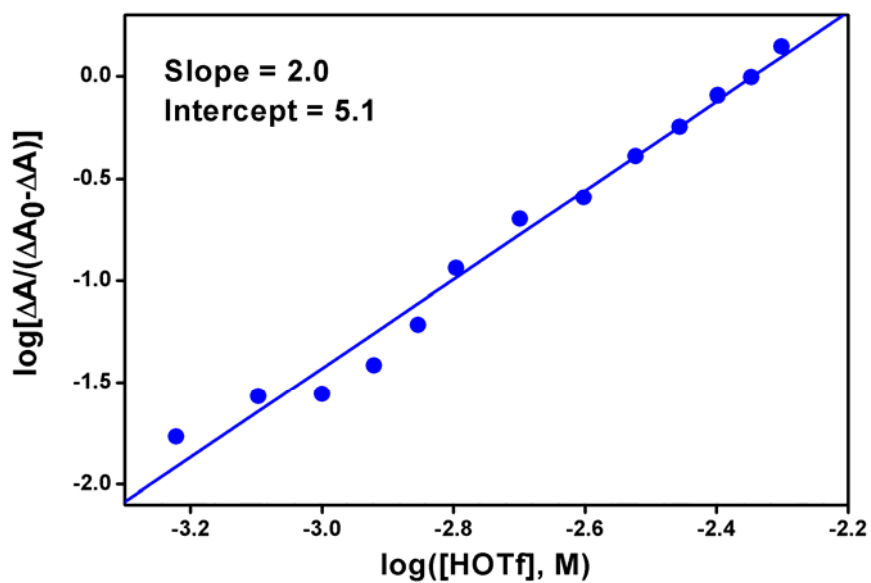
Fig. S2 Plot of $\log(\Delta A/(\Delta A_0 - \Delta A))$ against $\log[\text{HOTf}]$ in the spectral titration of **1** with HOTf. ΔA and ΔA_0 are the absorption change and the final absorption change, respectively, due to binding of n molecules of HOTf to **1** (see eqn (1) and (2); see also Fig. 2 in Text).
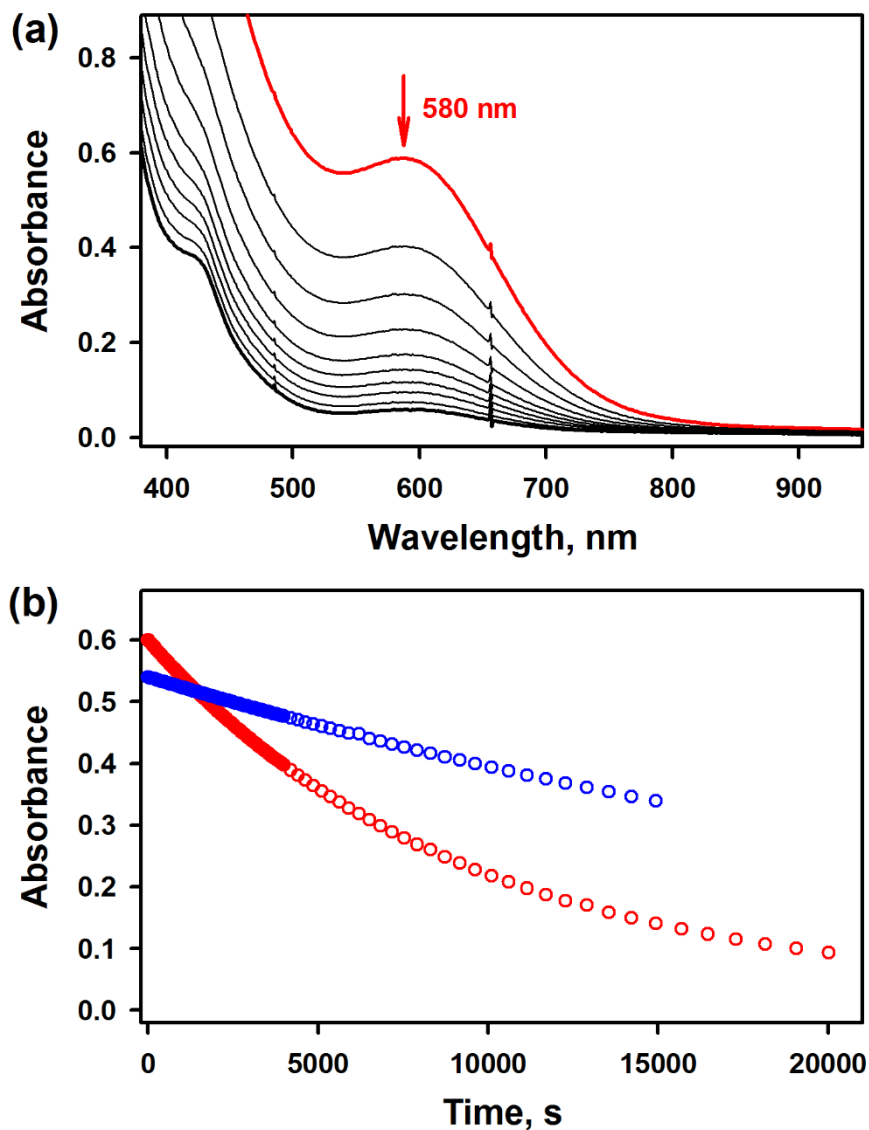
Fig. S3 (a) UV-vis spectral changes showing the natural decay of **4** (1.0 mM) in CF$_3$CH$_2$OH-CH$_3$CN (v/v = 1:1) at 273 K. (b) Time courses of the natural decays of **3** (1.0 mM; blue circles) and **4** (1.0 mM; red circles) monitored at 550 and 580 nm, respectively, in CF$_3$CH$_2$OH-CH$_3$CN (v/v = 1:1) at 273 K. The natural decay rates of **3** and **4** were 3.2×10^{-5} s^{-1} and 1.1×10^{-4} s^{-1}, respectively, at 273 K.
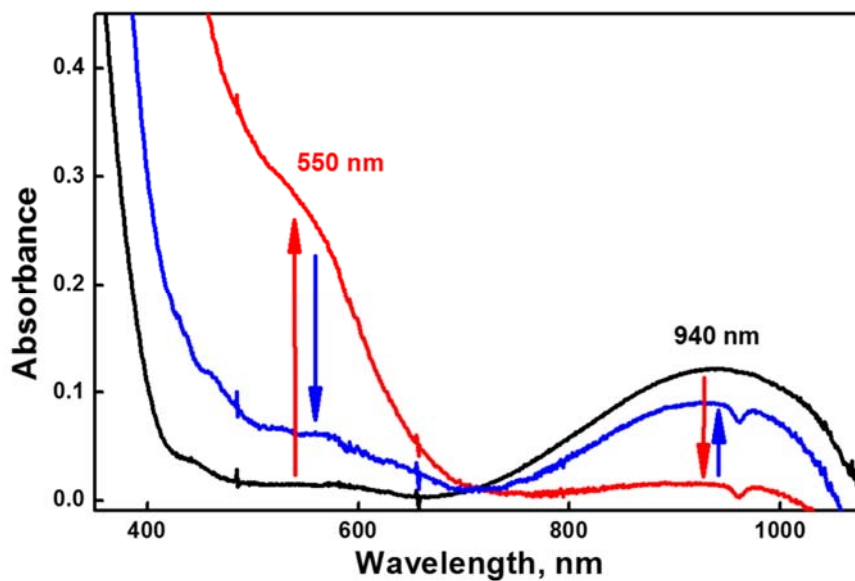
Fig. S4 UV-Vis spectra of **1** (0.50 mM; black line) and **3** (0.50 mM; red line) in CF$_3$CH$_2$OH-CH$_3$CN (*v/v* = 1:1) at 273 K. **3** was generated by adding 30 mM of HOTf to a solution of **1**. Blue line shows UV-vis spectrum of the reaction solution of **3** (0.50 mM) with triethylamine (30 mM) in CF$_3$CH$_2$OH-CH$_3$CN (*v/v* = 1:1) at 273 K.
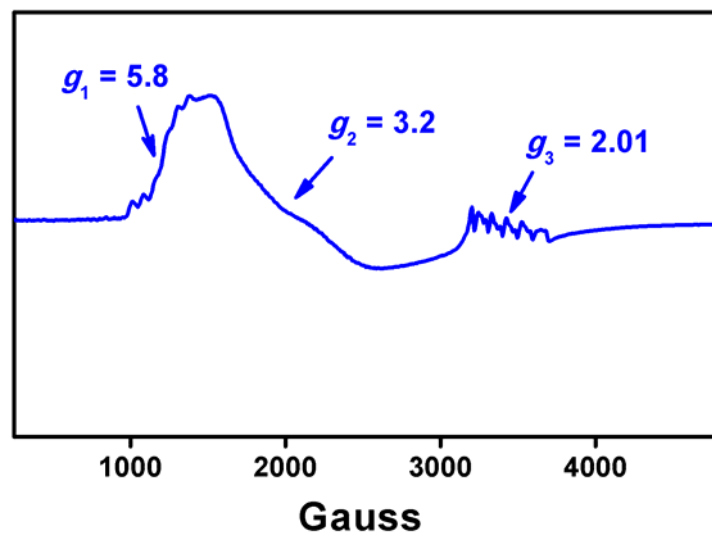
Fig. S5 X-band CW-EPR spectrum of $[(N4Py)Mn^{IV}(O)]^{2+}-(HOTf)_2$ (**3**) (2.0 mM) in the presence of HOTf (30 mM) in CF_3CH_2OH-CH_3CN (v/v = 1:1) in perpendicular mode at 5 K. The signals of g_1 = 5.8, g_2 = 3.2 and g_3 = 2.01 are characteristic of S = 3/2 Mn^{IV}.
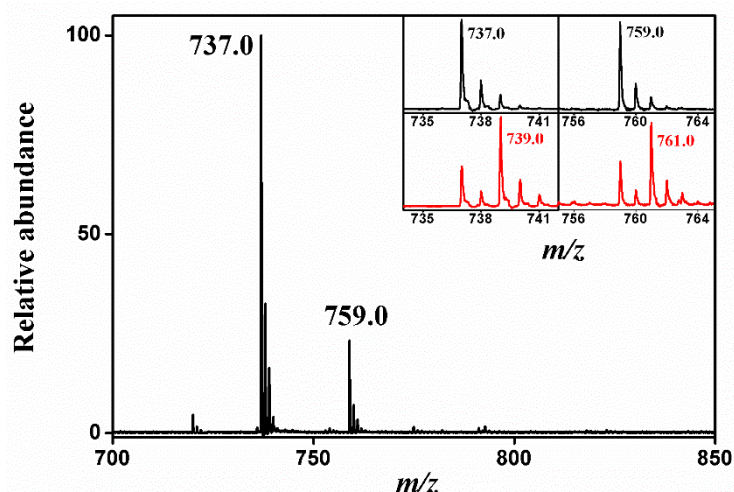
Fig. S6 CSI-TOF MS spectrum of **3** with HOTf (30 mM) in CF_3CH_2OH-CH_3CN (*v/v* = 1:1) at 273 K. The mass and isotope distribution patterns of ion peaks at *m/z* = 737.0 and 759.0 correspond to $[Mn^{IV}(O)(N4Py)(CF_3SO_3)(CF_3SO_3H)]^+$ (*calcd. m/z* = 737.1) and $[Mn^{IV}(O)(N4Py)(CF_3SO_3)(NaCF_3SO_3)]^+$ (*calcd. m/z* = 759.0), respectively. Insets show the observed isotope distribution patterns for **3**-^{16}O (upper panel) and **3**-^{18}O (lower panel). **1**-^{16}O (1.0 mM) and **1**-^{18}O (1.0 mM) were prepared by reacting $[(N4Py)Mn(CF_3SO_3)]^+$ (1.0 mM) with $PhI^{16}O$ (4.0 mM) and $PhI^{18}O$ (4.0 mM), respectively, and then **3**-^{16}O and **3**-^{18}O were generated upon addition of HOTf (30 mM) into the solution of **1**-^{16}O (1.0 mM) and **1**-^{18}O (1.0 mM). The peak at 759.0 is assigned to $[\mathbf{1}\text{-}NaCF_3SO_3]^+$, in which the Na^+ ion might be from the CSI-TOF MS conditions.
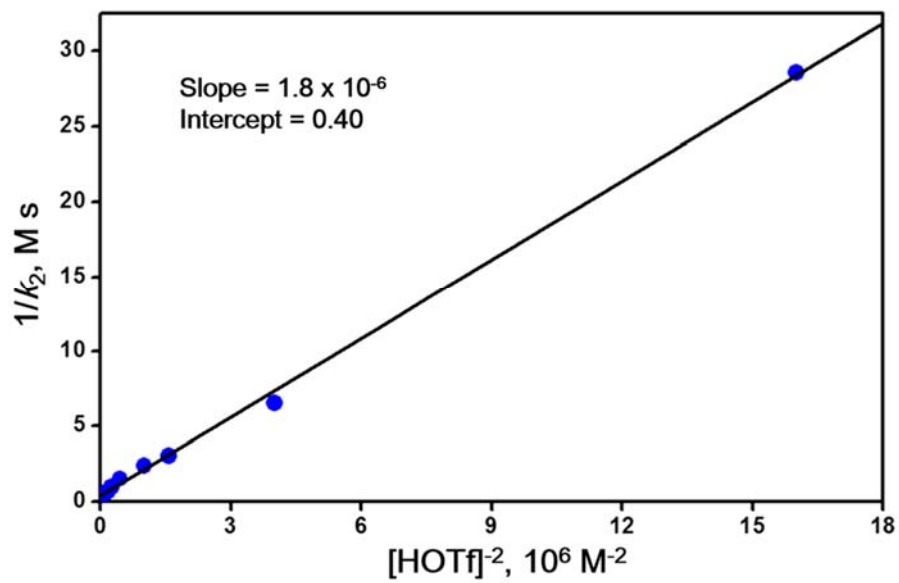
Fig. S7 Plot of $1/k_2$ (M s) for sulfoxidation of *para*-CN-thioanisole by **3** (0.50 mM) *vs.* $[HOTf]^{-2}$.
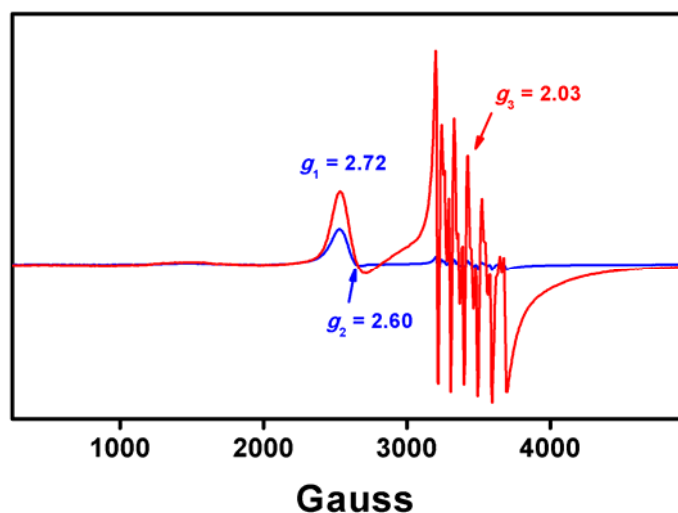
Fig. S8 X-band CW-EPR spectra of the resulting solutions obtained in the reactions of **3** (2.0 mM) with $[Ru^{II}(5\text{-}NO_2\text{-}phen)_3]^{2+}$ [2.0 mM (blue line) and 20 mM (red line)] after 4 h in the presence of HOTf (30 mM) in $CF_3CH_2OH\text{-}CH_3CN$ (v/v = 1:1) at 273 K. EPR spectra were recorded in perpendicular mode at 5 K. The EPR parameters of g_1 = 2.72 and g_2 = 2.60 in blue line are the signals of $[Ru^{III}(5\text{-}NO_2\text{-}phen)_3]^{3+}$; however, no signals of Mn^{II} species were detected, indicating Mn^{III} species was formed as a product.
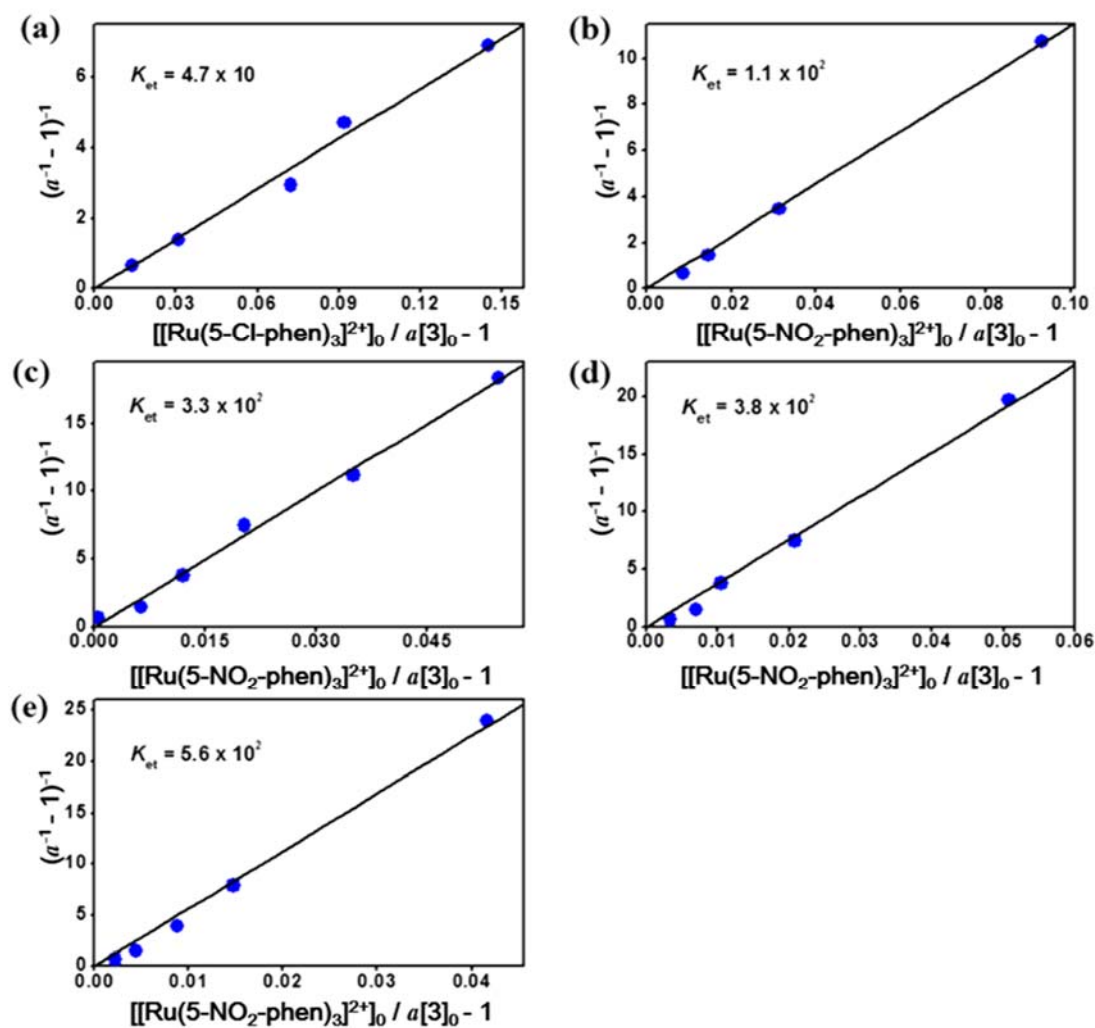
Fig. S9 (a) Plot of $(\alpha^{-1} - 1)^{-1}$ *vs.* $[[Ru^{II}(5\text{-Cl-phen})_3]^{2+}]_0/\alpha[\mathbf{3}]_0 - 1$ to determine the equilibrium constant, K_{et} ($K_{et} = [[Ru^{III}]^{3+}][[Mn^{III}(O)]^+]/[[Ru^{II}]^{2+}][[Mn^{IV}(O)]^{2+}]$), for electron transfer from $[Ru^{II}(5\text{-Cl-phen})_3]^{2+}$ to **3** upon addition of $[Ru^{II}(5\text{-Cl-phen})_3]^{2+}$ (0 − 1.0 mM) into a solution of **3** (0.50 mM) in the presence of HOTf (10 mM) in $CF_3CH_2OH\text{-}CH_3CN$ (*v/v* = 1:1) at 273 K ($\alpha = [[Ru^{III}]^{3+}]/[\mathbf{3}]_0$). (b, c, d, e) Plots of $(\alpha^{-1} - 1)^{-1}$ *vs.* $[[Ru^{II}(5\text{-NO}_2\text{-phen})_3]^{2+}]_0/\alpha[\mathbf{3}]_0 - 1$ to determine the equilibrium constants for electron transfer from $[Ru^{II}(5\text{-NO}_2\text{-phen})_3]^{2+}$ to **3** upon addition of $[Ru^{II}(5\text{-NO}_2\text{-phen})_3]^{2+}$ (0 − 1.0 mM) into a solution of **3** (0.50 mM) in the presence of HOTf [(b) 20 mM, (c) 30 mM, (d) 50 mM and (e) 80 mM] in $CF_3CH_2OH\text{-}CH_3CN$ (*v/v* = 1:1) at 273 K ($\alpha = [[Ru^{III}]^{3+}]/[\mathbf{3}]_0$).

Electronic Supplementary Information S18
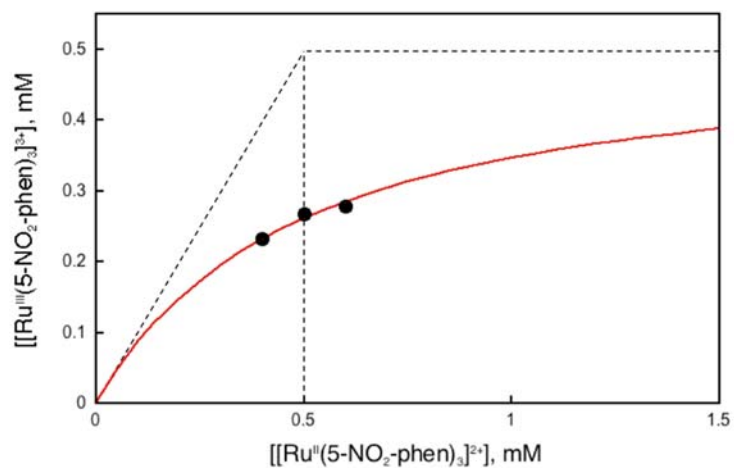
Fig. S10 Plot of concentration of $[Ru^{III}(5\text{-}NO_2\text{-}phen)_3]^{3+}$ produced in electron transfer from $[Ru^{II}(5\text{-}NO_2\text{-}phen)_3]^{2+}$ (1.50 V *vs.* SCE) to $[(Bn\text{-}TPEN)Mn^{IV}(O)]^{2+}$ (0.50 mM) in the presence of HOTf (30 mM) in $CF_3CH_2OH\text{-}CH_3CN$ (*v/v* = 1:1) at 273 K. The equilibrium constant (K_{et}) is determined to be 1.2.
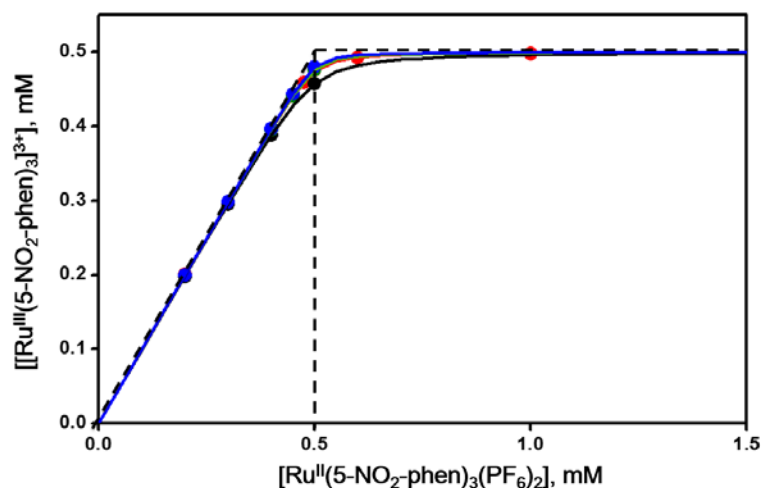
Electronic Supplementary Information S19

Fig. S11 Plots of concentration of $[Ru^{III}(5\text{-}NO_2\text{-}phen)_3]^{3+}$ produced in electron transfer from $[Ru^{II}(5\text{-}NO_2\text{-}phen)_3]^{2+}$ (1.50 V *vs*. SCE) to $[(N4Py)Mn^{IV}(O)]^{2+}$ (0.50 mM) in the presence of various HOTf concentrations (black circles, 20 mM; red circles, 30 mM; green circles, 50 mM; blue circles, 80 mM) *vs*. initial concentrations of $[Ru^{II}(5\text{-}NO_2\text{-}phen)_3]^{2+}$ in $CF_3CH_2OH\text{-}CH_3CN$ (*v/v* = 1:1) at 273 K.
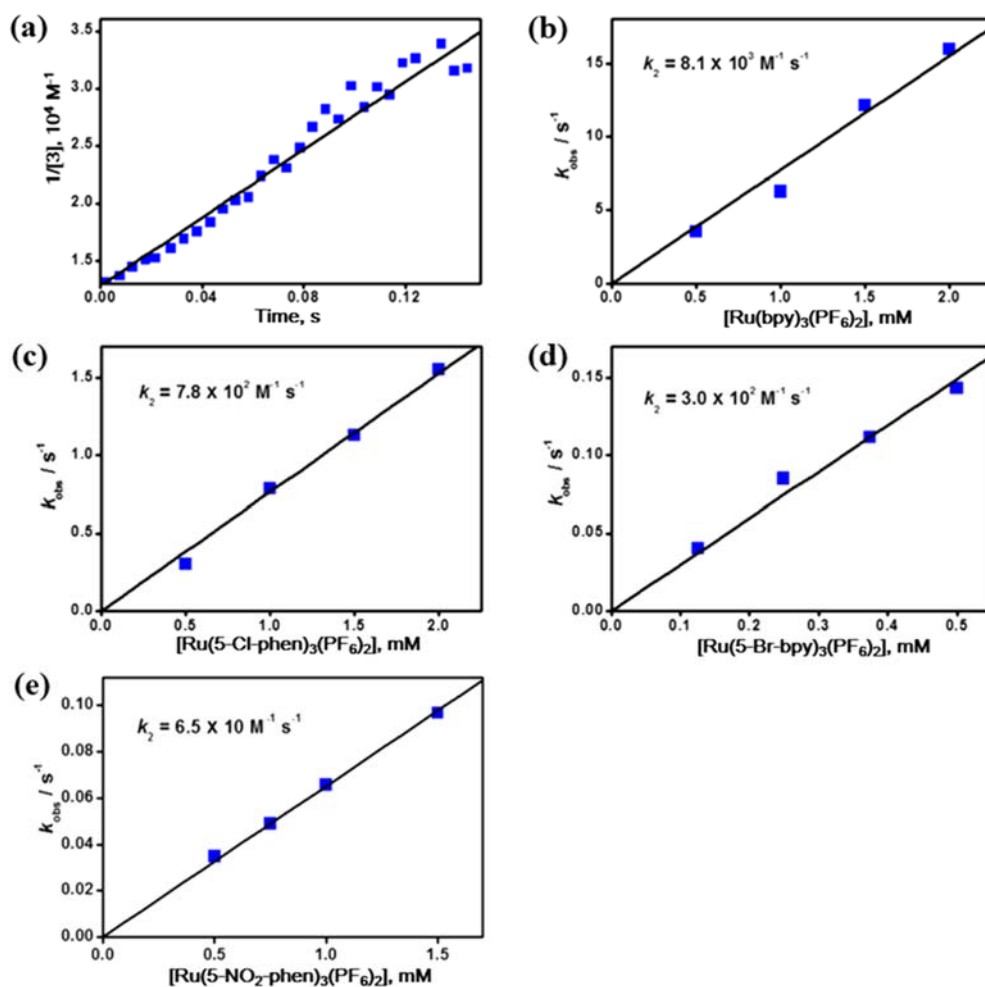
Fig. S12 (a) Second-order plot of $1/[\mathbf{3}]$ *vs.* time for electron transfer from $[Ru^{II}(Me_2\text{-}bpy)_3]^{2+}$ (0.10 mM) to **3** (0.10 mM). (b, c, d, e) Plots of k_{obs} against the concentration of one-electron reductants to determine second-order rate constants in the electron transfer reactions from one electron reductants [(b) $[Ru^{II}(bpy)_3]^{2+}$, (c) $[Ru^{II}(5\text{-}Cl\text{-}phen)_3]^{2+}$, (d) $[Ru^{II}(5\text{-}Br\text{-}bpy)_3]^{2+}$ and (e) $[Ru^{II}(5\text{-}NO_2\text{-}phen)_3]^{2+}$] to **3** in the presence of HOTf (30 mM) in $CF_3CH_2OH\text{-}CH_3CN$ (*v/v* = 1:1) at 273 K.
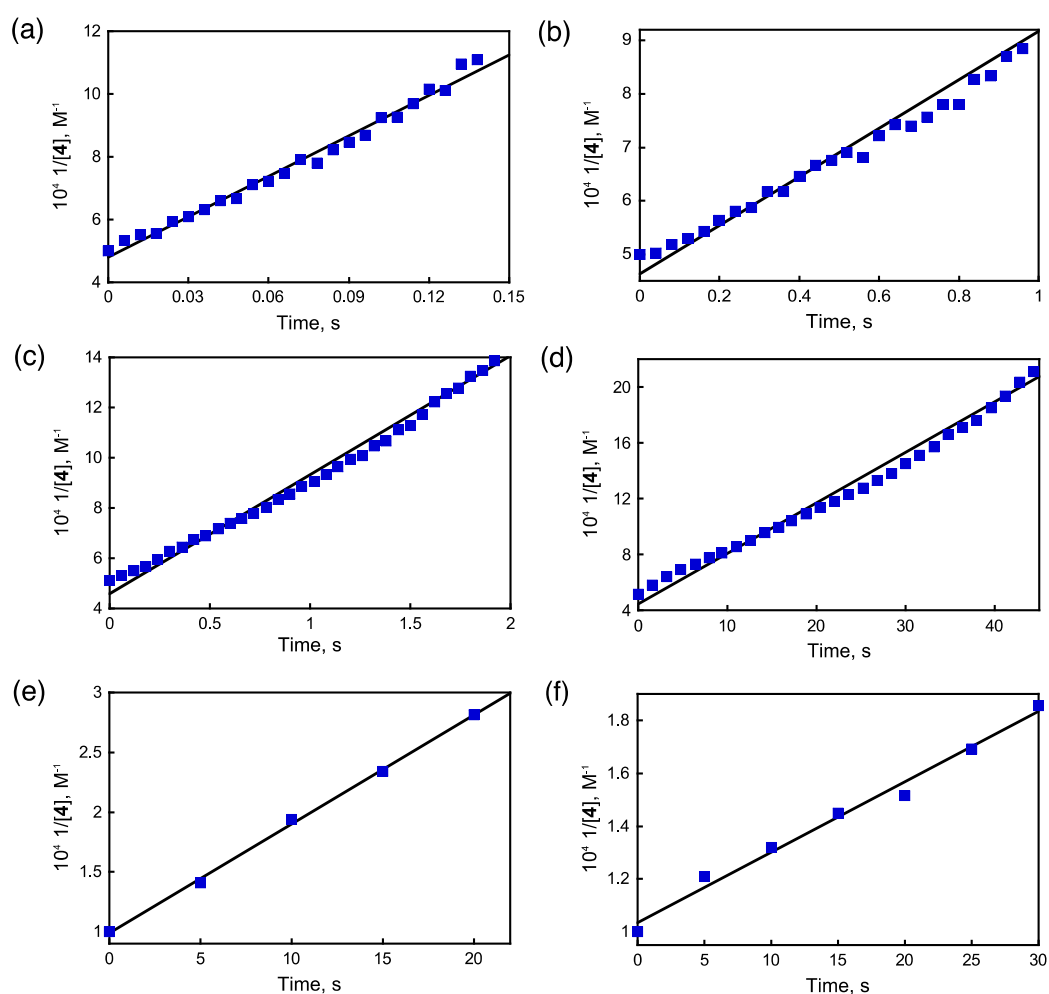
Fig. S13 Second-order plots of 1/[**4**] *vs.* time for electron transfer from one electron reductants (0.020 mM; (a) [Fe^{II}(Me$_2$-bpy)$_3$]$^{2+}$, (b) [Fe^{II}(phen)$_3$]$^{2+}$, (c) [Fe^{II}(bpy)$_3$]$^{2+}$, (d) [[Ru^{II}(Me$_2$-bpy)$_3$]$^{2+}$, (e) [Ru^{II}(5-Br-bpy)$_3$]^2 and (f) [Ru^{II}(5-Cl-phen)$_3$]$^{2+}$) to **4** (0.020 mM) in the presence of HOTf (30 mM) in CF$_3$CH$_2$OH-CH$_3$CN (*v/v* = 1:1) at 273 K.
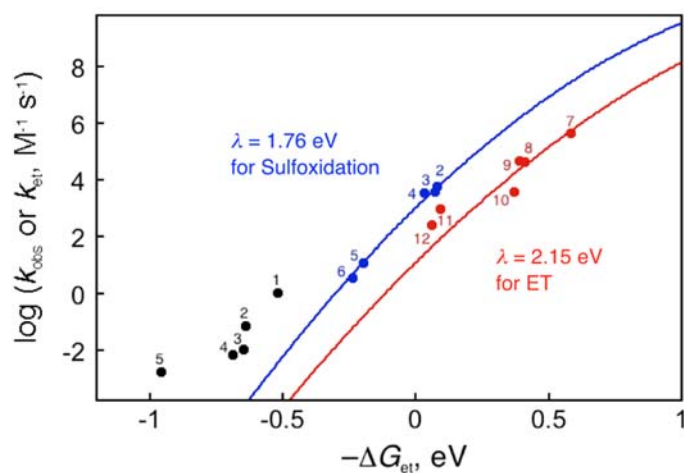
Fig. S14 Plots of log k_2 for sulfoxidation of *para*-X-substituted thioanisoles [X = (1) Me, (2) H, (3) F, (4) Br, (5) CN and (6) NO$_2$] by [(Bn-TPEN)Mn^{IV}(O)]$^{2+}$ (**2**; black circles) and [(Bn-TPEN)Mn^{IV}(O)]$^{2+}$−(HOTf)$_2$ (**4**; blue circles) *vs*. the driving force of electron transfer [$-\Delta G_{et} = e(E_{red} − E_{ox})$] from thioanisoles to **2** (E_{red} = 0.78 V *vs*. SCE) and **4** (E_{red} = 1.50 V *vs*. SCE) in the presence of HOTf (30 mM) in CF$_3$CH$_2$OH-CH$_3$CN (v/v = 1:1) at 273 K. The red circles show the driving force dependence of the rate constants (log k_2) of ET from one-electron reductants [(7) [Fe^{II}(Me$_2$-bpy)$_3$]$^{2+}$, (8) [Fe^{II}(bpy)$_3$]$^{2+}$, (9) [Fe^{II}(phen)$_3$]$^{2+}$, (10) [Ru^{II}(Me$_2$-bpy)$_3$]$^{2+}$, (11) [Ru^{II}(5-Cl-phen)$_3$]$^{2+}$ and (12) [Ru^{II}(Br-bpy)$_3$]$^{2+}$] to **4** in CF$_3$CH$_2$OH-CH$_3$CN (v/v = 1:1) at 273 K. The blue and red lines are the Marcus lines calculated with λ values of 1.76 and 2.15 eV, respectively.

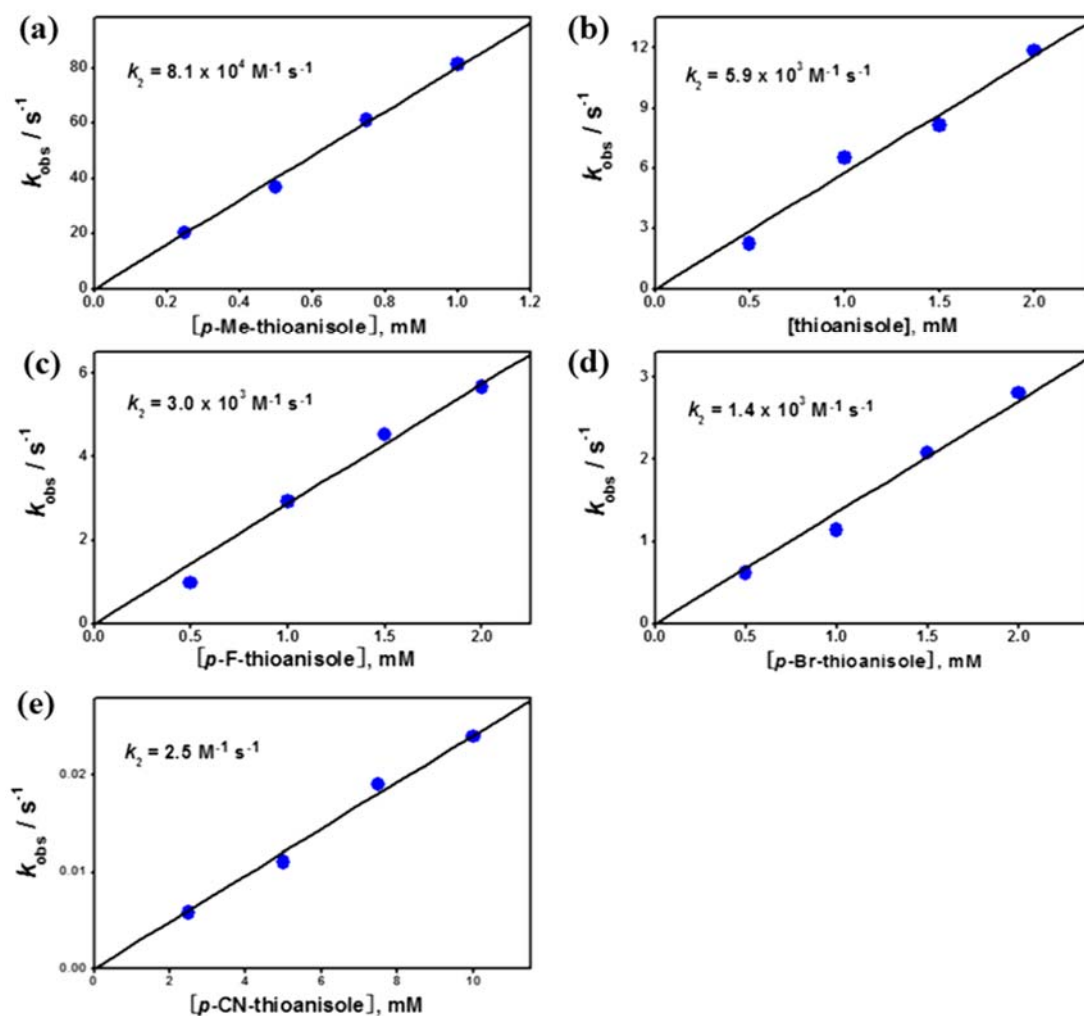Electronic Supplementary Information S23

Fig. S15 Plots of k_{obs} against the concentration of *para*-X-thioanisoles to determine second-order rate constants (k_2) in the oxidation of *para*-X-thioanisoles [X = (a) Me, (b) H, (c) F, (d) Br and (e) CN] by **3** in the presence of HOTf (30 mM) in CF_3CH_2OH-CH_3CN (v/v = 1:1) at 273 K.
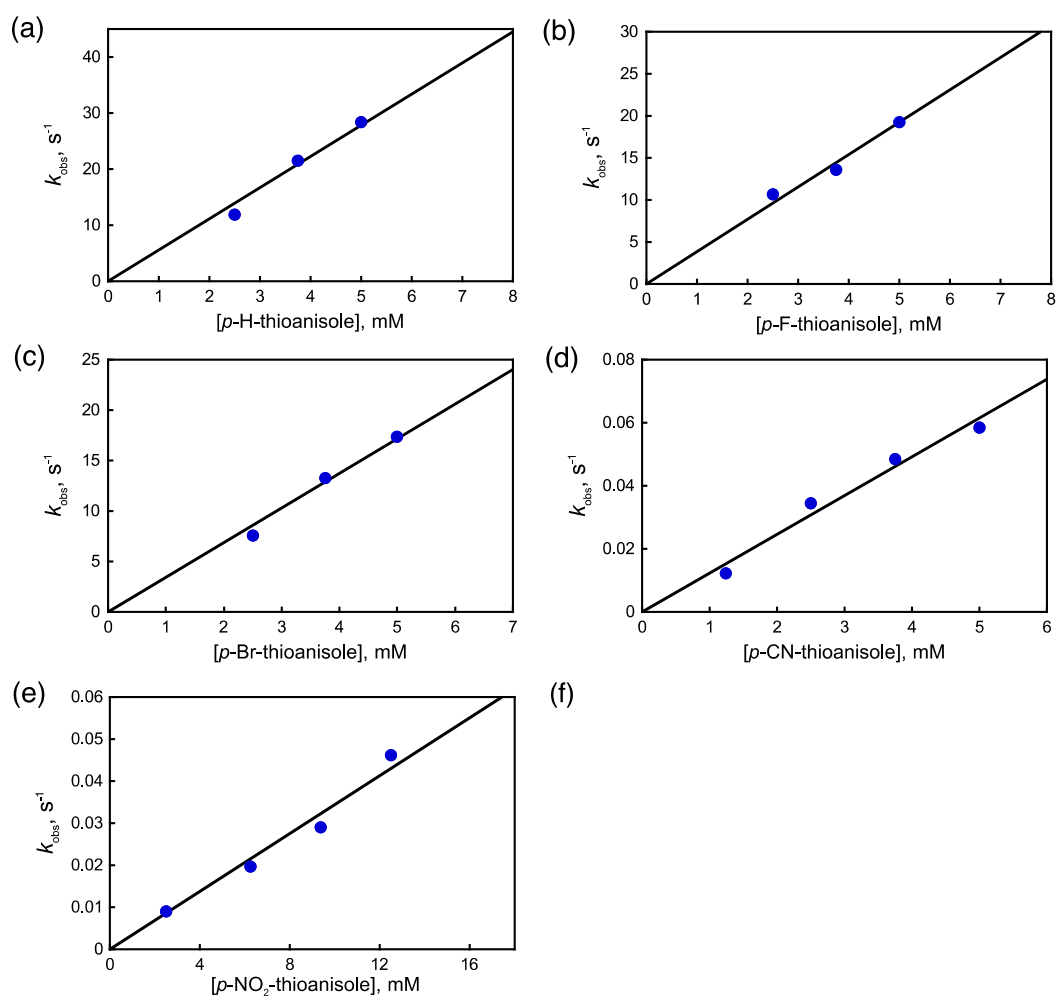
Fig. S16 (a) Plots of the pseudo-first-order rate constants (k_{obs}) of *para*-X-substituted thioanisoles [X = (a) H, (b) F, (c) Br, (d) CN and (e) NO$_2$] at 580 nm due to the decay of [(Bn-TPEN)Mn^{IV}(O)]$^{2+}$−(HOTf)$_2$ in the presence of HOTf (30 mM) in CF$_3$CH$_2$OH-CH$_3$CN (*v/v* = 1:1) at 273 K.
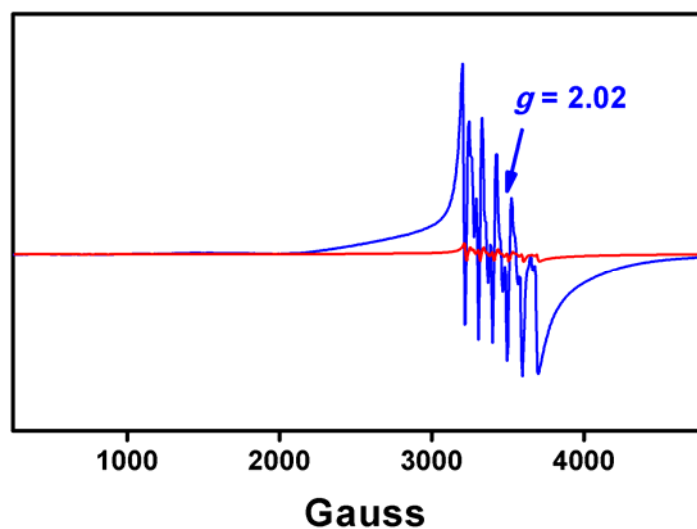
Fig. S17 X-band EPR spectra of reaction solutions of $[(N4Py)Mn^{IV}(O)]^{2+}-(HOTf)_2$ (**3**, 2.0 mM) with thioanisole (20 mM; blue line) and 1,4-cyclohexadiene (20 mM; red line) in the presence of HOTf (30 mM) in CF_3CH_2OH-CH_3CN ($v/v = 1:1$) at 273 K and 298 K, respectively. EPR spectra were recorded in perpendicular mode at 5 K.
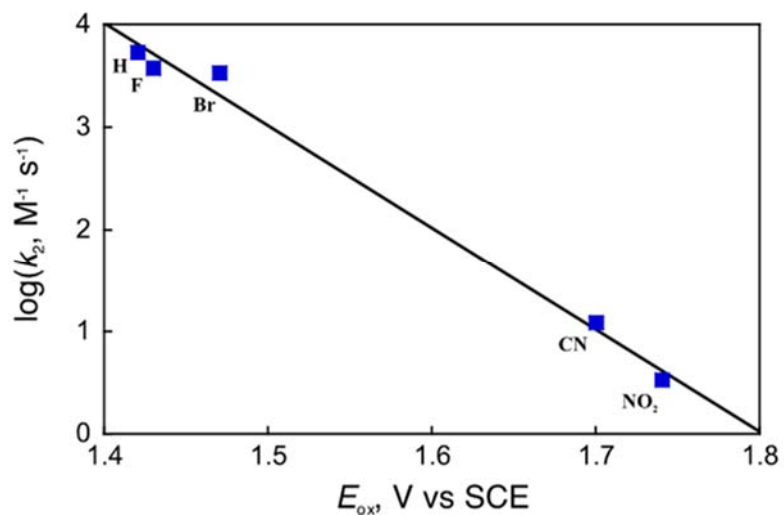
Fig. S18 Plot of log k_2 against the one-electron oxidation potentials (E_{ox}) of *para*-X-thioanisoles (X = H, F, Br, CN and NO$_2$) by [(Bn-TPEN)Mn^{IV}(O)]$^{2+}$−(HOTf)$_2$ [slope = −10.0(6)] in the presence of HOTf (30 mM) in CF$_3$CH$_2$OH-CH$_3$CN (*v/v* = 1:1) at 273 K.
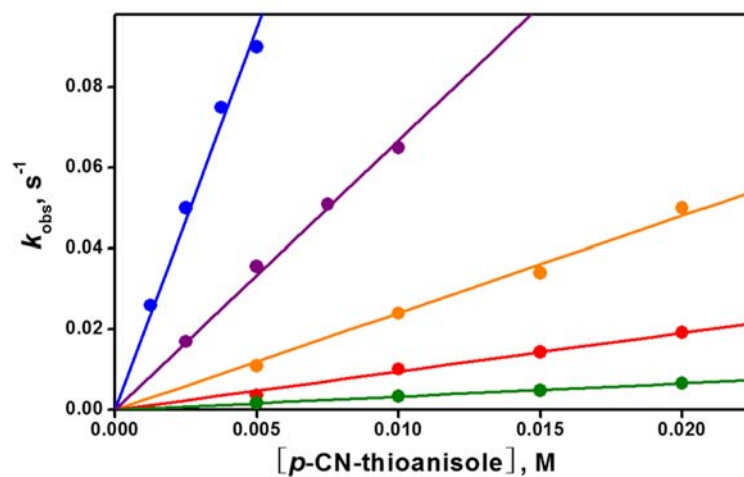
Fig. S19 Plots of k_{obs} against the concentration of *para*-CN-thioanisole to determine second-order rate constants (k_2) in the oxidation of *para*-CN-thioanisole by **3** in the presence of HOTf (30 mM) in CF_3CH_2OH-CH_3CN (v/v = 1:1) at various temperature [293 K (blue), 283 K (violet), 273 K (orange), 263 K (red) and 253 K (green)].
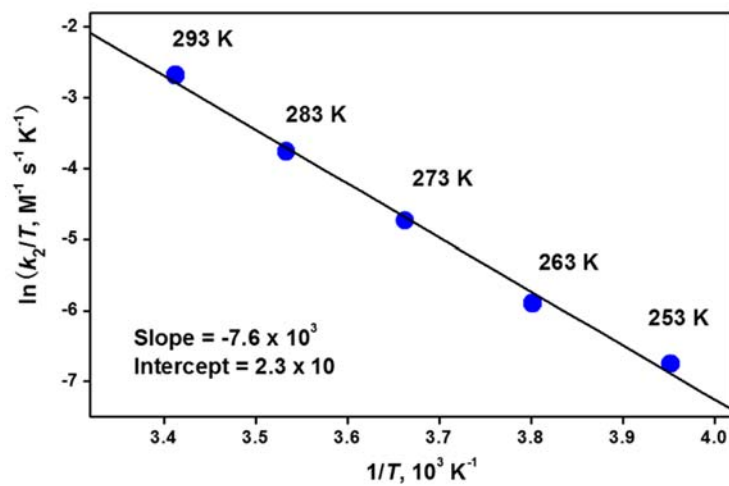
Fig. S20 Eyring plot to determine activation parameters for the reaction of **3** with *para*-CN-thioanisole in the presence of HOTf (30 mM) in CF_3CH_2OH-CH_3CN (*v/v* = 1:1).
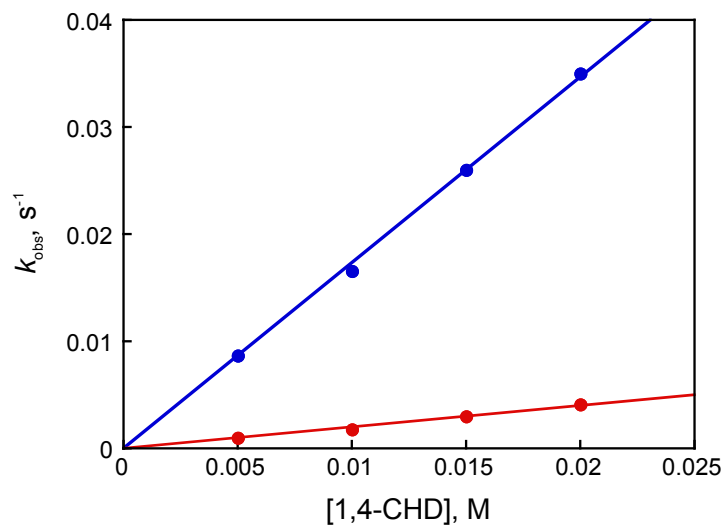
Fig. S21 Plots of k_{obs} against the concentration of 1,4-cyclohexadiene (CHD) to determine the second-order rate constants in the oxidation of CHD by **2** (0.25 mM) and **4** (0.25 mM) in CF_3CH_2OH-CH_3CN (v/v = 1:1) at 273 K, respectively. Deceleration (~9-fold) of C-H bond activation by $[(Bn\text{-}TPEN)Mn^{IV}(O)]^{2+}$−$(HOTf)_2$ can be explained as prohibiting suitable interaction between Mn(IV)-oxo moiety and CHD.